

NiO_x Supported PtRh Nanoalloy Enables High-Performance Hydrogen Evolution Reaction in Universal pH Conditions

Dinesh Bhalothia ^a, Yu-Min Yu ^b, Yi-Ru Lin ^b, Tzu-Hsi Huang ^b, Che Yan ^a, Jyh-Fu Lee ^c, Kuan-Wen
Wang, ^{b*} and Tsan-Yao Chen^{a,d,e,f*}

Affiliations:

^a Department of Engineering and System Science, National Tsing Hua University, Hsinchu 30013, Taiwan

^b Institute of Materials Science and Engineering, National Central University, Taoyuan City 32001, Taiwan

^c National Synchrotron Radiation Research Center, Hsinchu 30076, Taiwan

^d Institute of Nuclear Engineering and Science, National Tsing Hua University, Hsinchu 30013, Taiwan

^e Hierarchical Green-Energy Materials (Hi-GEM) Research Centre, National Cheng Kung University, Tainan 70101, Taiwan

^f Department of Materials Science and Engineering, National Taiwan University of Science and Technology, Taipei 10617, Taiwan

Corresponding Author(s):

Kaung-Wen Wang

Email: kuanwen.wang@gmail.com

Tsan-Yao Chen

Email: chencaeser@gmail.com

Tel: +886-3-5715131 # 34271

FAX: +885-3-5720724

1. Physical Characterizations of Experimental NCs.

The physical characteristics of the experimental NCs were unravelled by cross-referencing results of microscopy and X-ray spectroscopic analysis. The exact atomic compositions of the catalysts were examined by an inductively coupled plasma-optical emission spectrometer (ICP-OES, Agilent 725) (**Table S1**). The particle size and surface morphologies of the experimental NCs were revealed by high-resolution transmission electron microscopy (HRTEM, JEOL JEM 2100F) equipped with a LaB₆ electron gun source with maximum accelerating voltages of 200 kV. The samples for HRTEM analysis were prepared via dispersing the catalyst powder into 2-propanol (IPA) and drop-casted on the 200 mesh copper grids. These specimens were then dried at 70 °C for 12 hours in the oven. Before loading into the HRTEM chamber, the specimens were cleaned by plasma to remove the contaminated species on the surface of the specimens. The phases and structures of the NCs under investigation were revealed by X-ray diffraction (XRD, Rigaku) using Cu K_α ($\lambda = 0.154$ nm) radiation operated at 40 kV and 25 mA. The patterns were measured ranging from 20 to 80° at a scan rate of 0.124° per step. Meanwhile, the average crystallite size (D) of the as-prepared NCs was estimated by Scherrer's equation (S1).

$$D = \frac{K\lambda}{FWHM \cos \theta} \dots (S1)$$

Where $\lambda = 0.154$ nm is the wavelength, $K = 0.89$ is the Scherrer constant, θ is the Bragg angle, and FWHM is the full width at half maximum.

The X-ray absorption spectroscopy (XAS) technique was applied to unveil the atomic arrangements and electronic states of the experimental NCs. The XAS spectra of experimental samples were obtained in transmission or fluorescence mode at the beamlines BL-01C1 and BL-17C at the National Synchrotron Radiation Research Center (NSRRC), Taiwan. The incident beam was monochromated using a double crystal monochromator equipped with a Si (111) crystal. A Si monochromator was employed to adequately select the energy with a resolution $\Delta E/E$ better than 10^{-4} at the Pt L_{II} -edge (13273 eV) and Pt L_{III} -edge (11564 eV). For

data collection, all the NCs were dispersed uniformly on the tape with an appropriate absorption thickness ($\mu x = 1.0$, where μ is the X-ray attenuation coefficient at the absorption edge and x is the thickness of the sample) to attain a proper edge jump step at the absorption edge region. The ionization chamber filled with different mixing gases such as Ar, N₂, He or Kr was used to detect the intensities of the incident beam (I_0), the fluorescence beam (I_f) and the beam finally transmitted through a reference foil (I_r) for X-ray energy calibration. To acquire acceptable quality spectra with good quality, each XANES measurement was repeated at least twice and averaged for successive comparisons. Further, based on the Pt L₃ spectra, the fractional change in the number of d-band vacancies relative to the reference material (f_d) was estimated according to the following equation:

$$f_d = \frac{\Delta A_3 + 1.11\Delta A_2}{(A_3 + 1.11A_2)_r} \dots (S2)$$

where ΔA_2 and ΔA_3 are expressed by

$$\Delta A_2 = A_{2s} - A_{2r} \text{ and } \Delta A_3 = A_{3s} - A_{3r} \dots (S3)$$

$\Delta A_2 = (A_{2s} - A_{2r})$ The terms A_2 and A_3 are the areas under L₂ and L₃ absorption edges of the sample (s) and reference (r) material. The d-band vacancies of Pt in the sample can be evaluated using the equation of relation. The value of unfilled d-states in the reference material (H_{Tr}) was evaluated from band structure calculations to be 0.3.

$$H_{Ts} = (1 + f_d)H_{Tr} \dots (S4)$$

Besides, the EXAFS analysis is carried out via subtracting the background of the pre/post-edge and subsequently normalizing with respect to the edge jump step from the XANES spectra ($\chi(E)$). The normalized $\chi(E)$ spectra were transformed from energy to k -space and further weighted by k^3 to discern the effect of backscattering interferences from different coordination shells. Subsequently, the extracted k^3 -weighted spectra in k -space ranging from 3.5 to 13.8 Å⁻¹ for the Pt L₃-edge was Fourier transformed (FT) into r -space. Finally,

the filtered EXAFS data of Pt L_{III}-edge was analyzed by a nonlinear least-squares curve fitting method in the *r*-space ranging from 1.0 to 3.1 Å⁻¹ depending on the bond to be fitted. The reference phase and amplitude for the Pt–Pt coordination were initially acquired from the Pt foil. Normally, the backscattered amplitude and phase shift functions for specific atom pairs were theoretically estimated by means of utilizing the FEFF7 code. Structural parameters such as bond distance (R) and coordination number (CN) had been computed. Additionally, the reduction amplitude value (S_0^2) for Pt was fixed at 0.9 to determine various structural parameters for each bond pair. The X-ray photoelectron spectroscopy (XPS, Thermo VG Scientific Sigma Probe) using a monochromatic X-ray source (Al K α) at a voltage of 20 kV and a current of 30 mA was used to investigate the oxidation states and surface compositions of catalysts. The base pressure in the analysing chamber was maintained at 10⁻⁹ Torr and all binding energies were calibrated with respect to the C 1s peak at 284.6 eV. The surface compositions of the catalysts were estimated by calculating the integral of each peak. Shirley type background was used to subtract the original peak and then a combination of Lorentzian and Gaussian lines was applied to fit the experimental curve.

2. Electrochemical Hydrogen Evolution Reaction Performance Analysis.

The electrochemical measurements were performed by using a CHI 611C potentiostat equipped with a three-electrode cell configuration, where a glassy carbon (0.196 cm²) and KCL saturated Ag/AgCl electrodes were used as a working electrode and reference electrode, respectively. Besides, a platinum wire was used as the counter electrode. All potentials in this study were referred to the normal hydrogen electrode (NHE) and the potential of Ag/AgCl electrode was +0.204 V versus that of NHE. The catalyst slurry for electrochemical measurements was prepared by ultrasonically dispersing 5 mg of catalyst powder into 1ml of isopropanol (IPA) and 50 µl of Nafion (5 wt. %, Dupont) solution for 1 h. The electrocatalytic performance of experimental NCs toward HER was estimated by conducting the linear sweep voltammetry (LSV) within the potential range from -0.20 and 0.20 V at a sweeping rate of 2 mV s⁻¹ and a rotation rate of 1600 rpm in N₂ saturated 0.5 M H₂SO₄ (for acidic HER) and 1M KOH (for alkaline HER) electrolyte. Beside, in order to estimate the catalytic activities of the PtRhNi-NCs for the neutral HER, RDE voltammetry was performed in N₂-saturated 1.0 M phosphate buffer solution (PBS) at an electrode rotation rate of 1600 rpm. For conducting the HER test, 40.0 µl of catalyst ink was drop cast and air-dried on the working electrode. Prior to each test, the electrode was cycled several times between 0.00 and 1.24 V in N₂ saturated 0.5 M H₂SO₄ and/or 1M KOH to gain a relatively stable and clean surface. The Tafel equation was used to describe the current–potential relationship at a significant overpotential (η):

$$\eta = a + b \log\left(\frac{j}{j_0}\right) \dots (S5)$$

where j is the current density, j_0 is the exchange current density, a is the Tafel intercept, and b is the Tafel slope. The Tafel slope and intercept were calculated by using the following equations:

$$a = \frac{-2.303RT}{\alpha zF} \log j_0 \dots (S6)$$

$$b = \frac{2.303RT}{\alpha zF} \dots (S7)$$

Where α is the electron transfer coefficient, z is the electron transfer number, F is the Faraday's constant, R is the ideal gas constant, T is the temperature. The durability of as-prepared NCs toward HER was measured by a chronoamperometric (CA) test at the potential of -50 mV for 12 h in a N_2 saturated 0.5 M H_2SO_4 and/or 1M KOH electrolyte.

The cyclic voltammetry (CV) analysis was employed to determine the electrochemical surface area (ECSA) of the experimental NCs based on the hydrogen adsorption/desorption region. The CV curves were measured within the potential range between 0.00 and 1.20 V at a sweeping rate of 20 $mV s^{-1}$ in N_2 -saturated 0.5 M H_2SO_4 and/or 1 M KOH aqueous solution. The ECSA was calculated by integrating the areas of H adsorption between 0.00 and 0.40 V after the deduction of the double-layer region. By using the charge passed for H- adsorption, Q_H , the ECSA was calculated using the following equation:

$$ECSA = \frac{Q_H}{[Pt] \times 0.21} \dots (S8)$$

where $[Pt]$ represents the platinum loading ($mg cm^{-2}$) on the electrode, Q_H represents the charge for H adsorption ($mC cm^{-2}$) and 0.21 is the charge required to oxidize a monolayer of H_2 on clean Pt.

In addition, the CO-stripping curves were obtained by purging CO gas in 0.5 M H_2SO_4 for 30 minutes prior to the experiment; while operating, CO was kept purging at -0.1 V (vs. SCE) for 30 minutes, then CO-stripping was measured between -0.3 and 0.76 V (vs. SCE) at the scan rate of 50 $mV s^{-1}$. The electrochemically active surface area calculated from CO-stripping ($ECSA_{CO}$) is defined by the equation (9):

$$ECSA_{CO} = \frac{Q_{CO}}{[Pt] \times 0.42} \dots (S9)$$

Where $[Pt]$ presents the Pt loading (mg/cm^2) on the electrode, Q_{CO} indicates the charge for CO-adsorption (C/cm^2) and 0.42 is assuming that the oxidation of a CO monolayer is required.

3. The ICP-OES determined exact compositions of the experimental NCs.

Table S1. The ICP-OES determined exact atomic compositions of the experimental NCs.

	Pt (wt%)	Rh (wt%)	Ni (wt%)
Pt	1.03	N/A	N/A
Rh	N/A	0.54	N/A
PtRh	0.95	1.43	N/A
PtRhNi	1.12	1.25	0.25

4. The Atomic-scale high angle annular dark field-STEM (HAADF-STEM) image of PtRhNi NC.

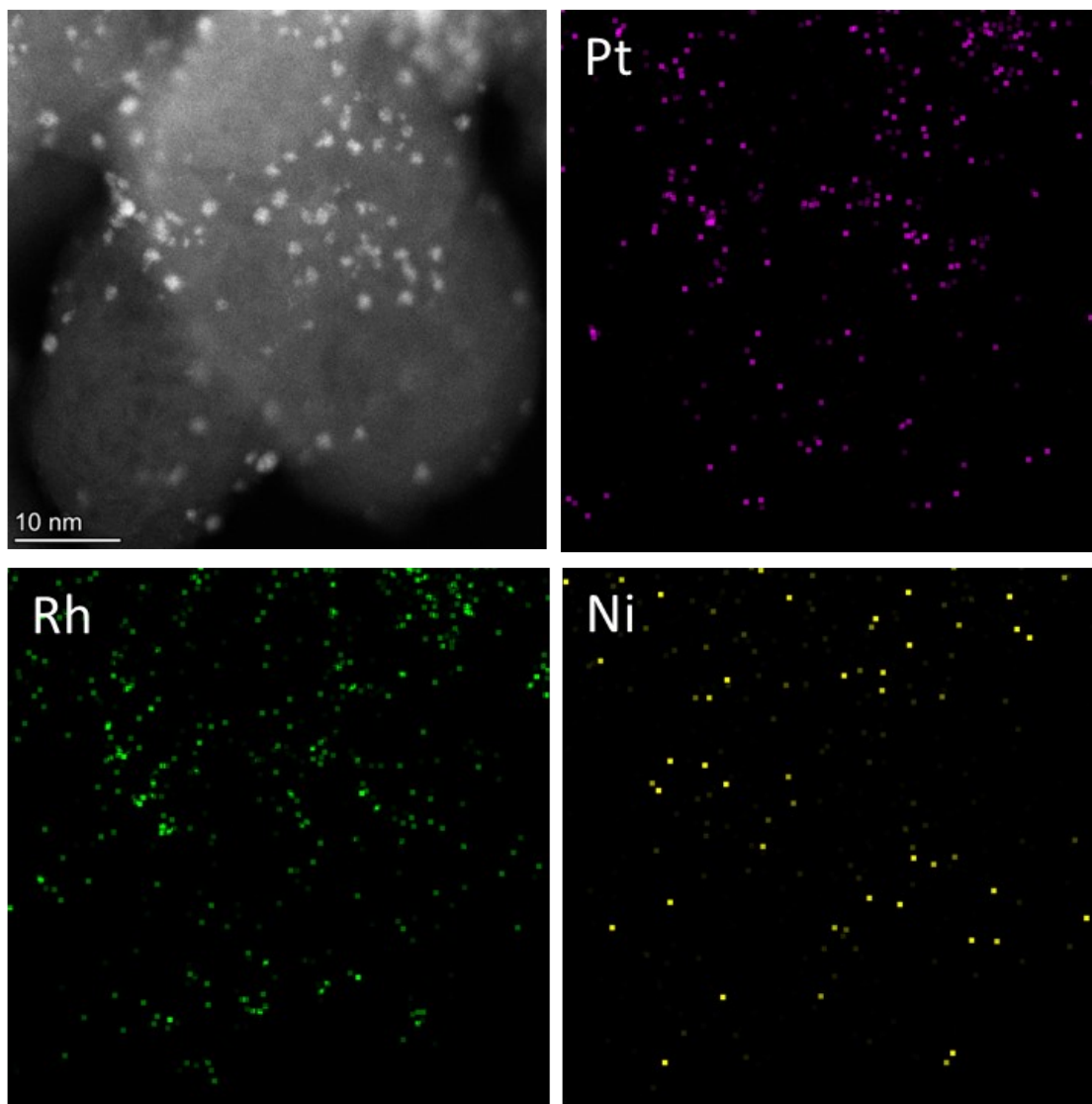


Figure S1. Atomic-scale high angle annular dark field-STEM (HAADF-STEM) image of PtRhNi NC.

5. The XRD patterns of Pt, Rh, PtRh, and PtRhNi-NCs.

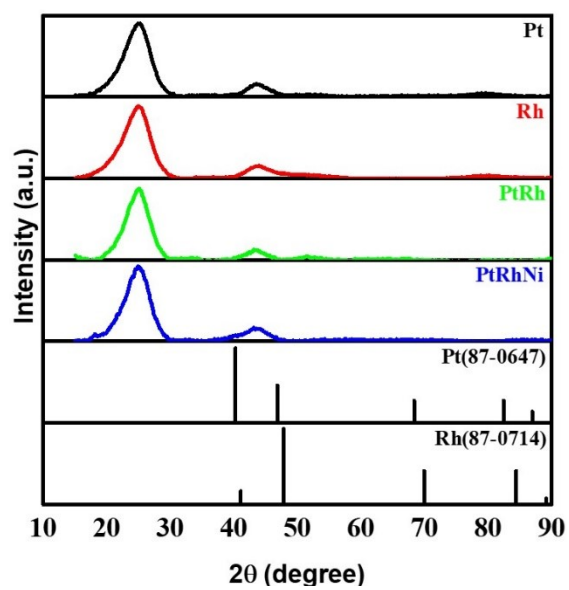


Figure S2. The XRD patterns of Pt, Rh, PtRh, and PtRhNi-NCs.

6. Normalized X-ray absorption near-edge spectroscopy (XANES) of the experimental NCs at Pt L₂-edge.

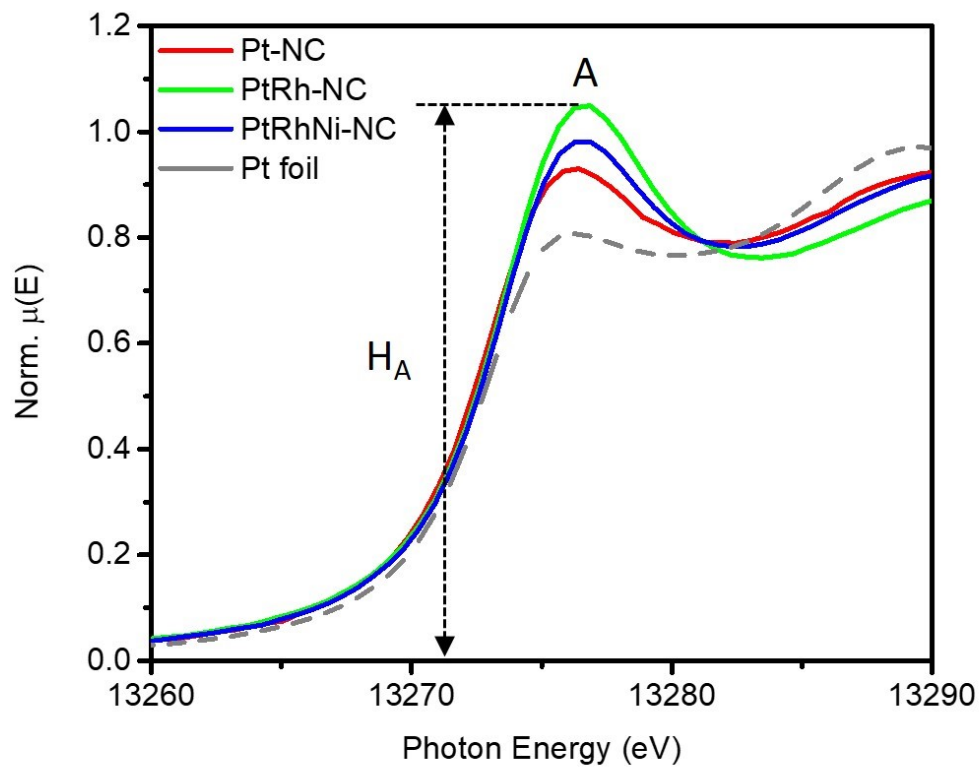


Figure S3. Normalized X-ray absorption near-edge spectroscopy (XANES) of the experimental NCs at Pt L₂-edge.

7. Model analysis fitting curves compared with experimental FT-EXAFS spectra at Pt L₃-edge of (a) Pt, (b) PtRh and (c) PtRhNi NC.

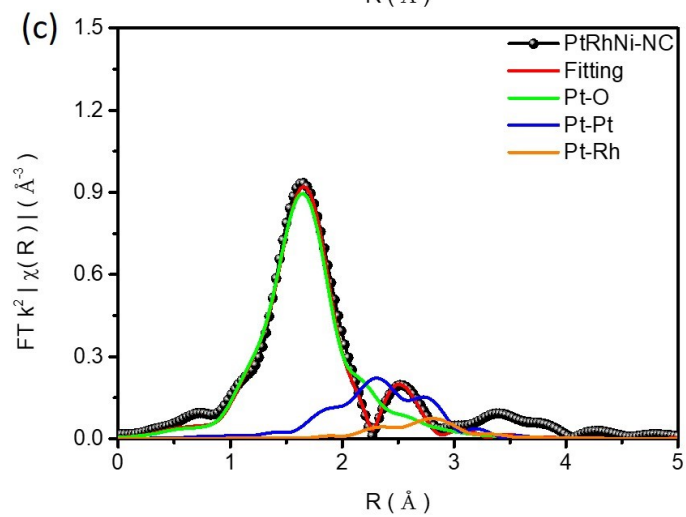
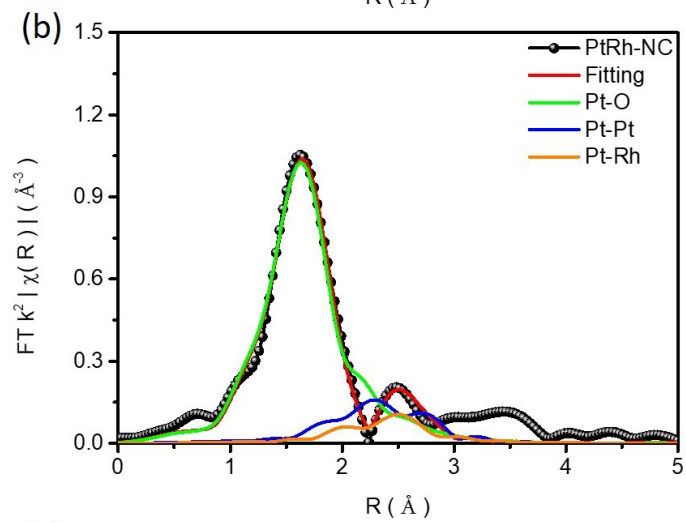
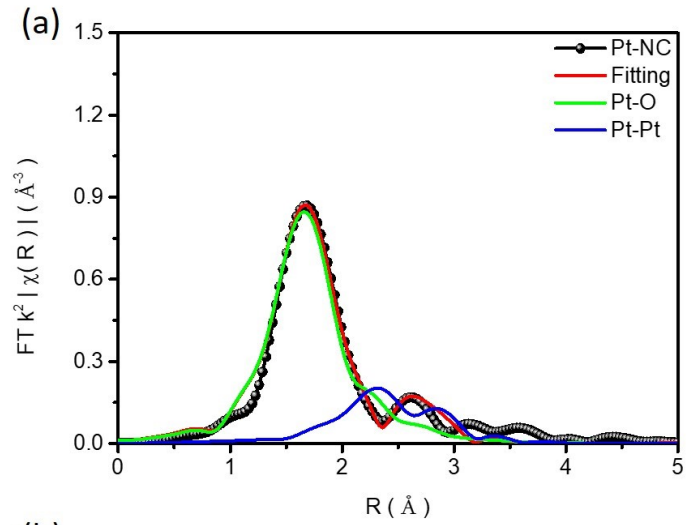


Figure S4. Model analysis fitting curves compared with experimental FT-EXAFS spectra at Pt L₃-edge of (a) Pt, (b) PtRh and (c) PtRhNi NC.

8. Model analysis fitting curves compared with experimental FT-EXAFS spectra at Rh K-edge of (a) Rh, (b) PtRh and (c) PtRhNi NC.

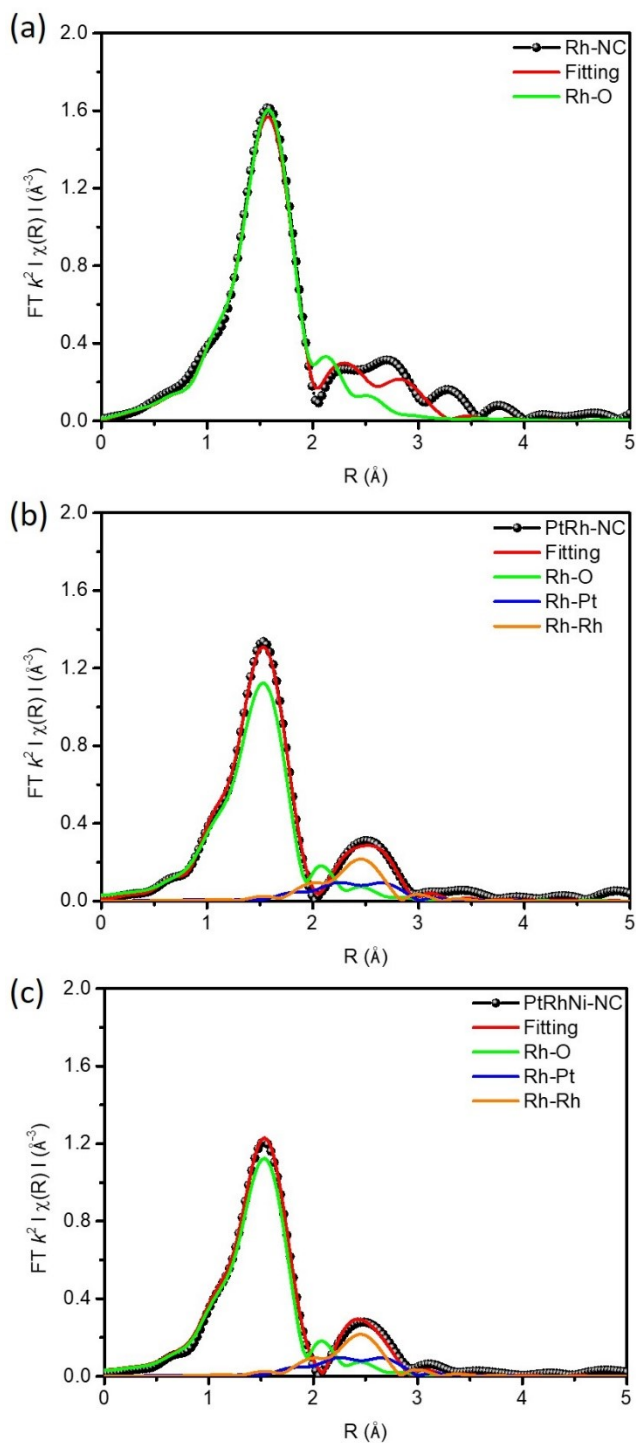


Figure S5. Model analysis fitting curves compared with experimental FT-EXAFS spectra at Rh K-edge of (a) Rh, (b) PtRh and (c) PtRhNi NC.

9. Comparative normalized XANES and FT-EXAFS spectra with fitting curves of the PtRhNi NC and Ni-foil at Ni K-edge.

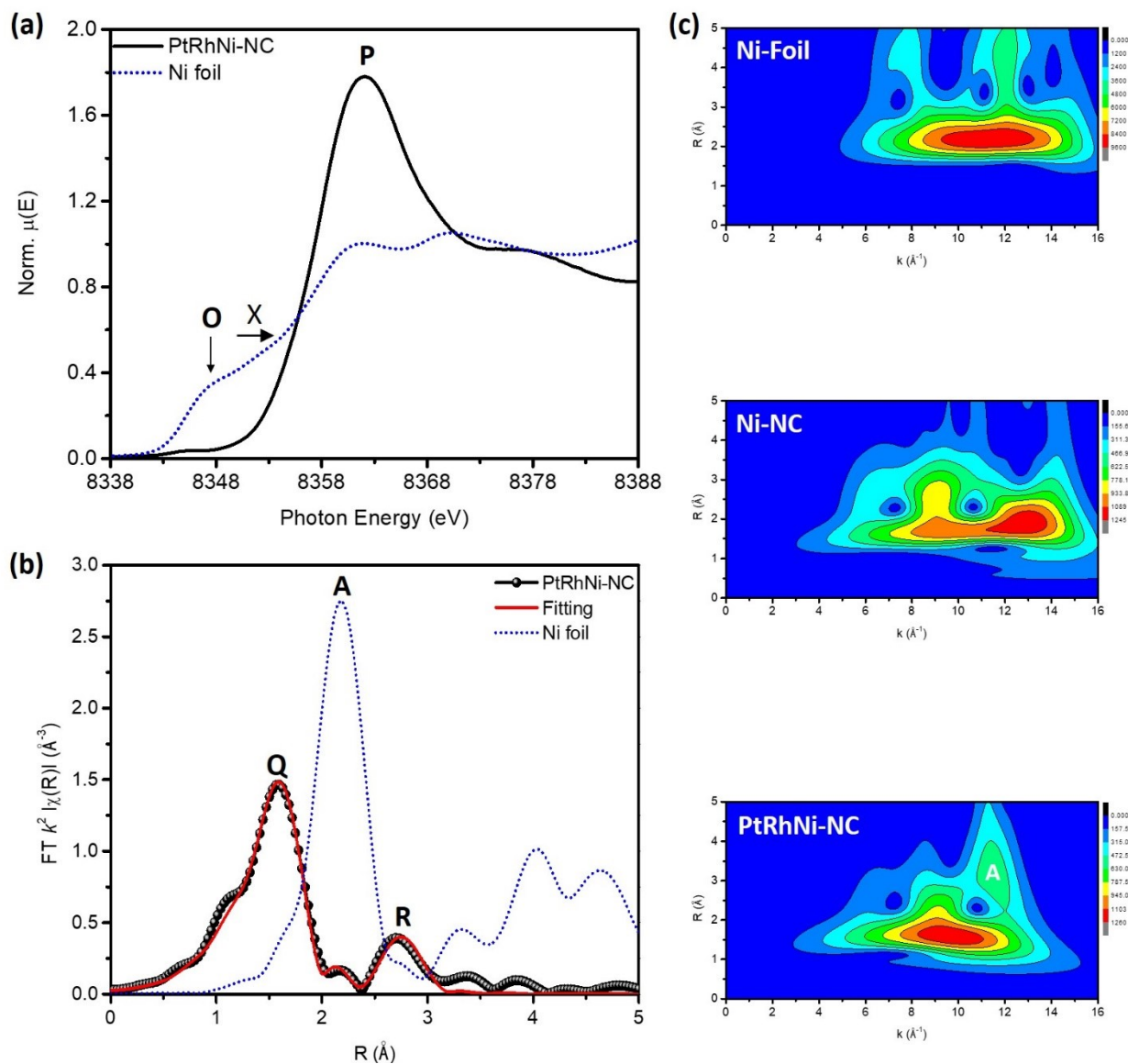


Figure S6. (a) Normalized XANES, (b) FT-EXAFS spectra and (c) the wavelet transformation plots for the k^2 -weighted EXAFS signals of the PtRhNi NC compared with Ni-foil at Ni K-edge.

10. The Full XPS spectrum of PtRhNi NC.

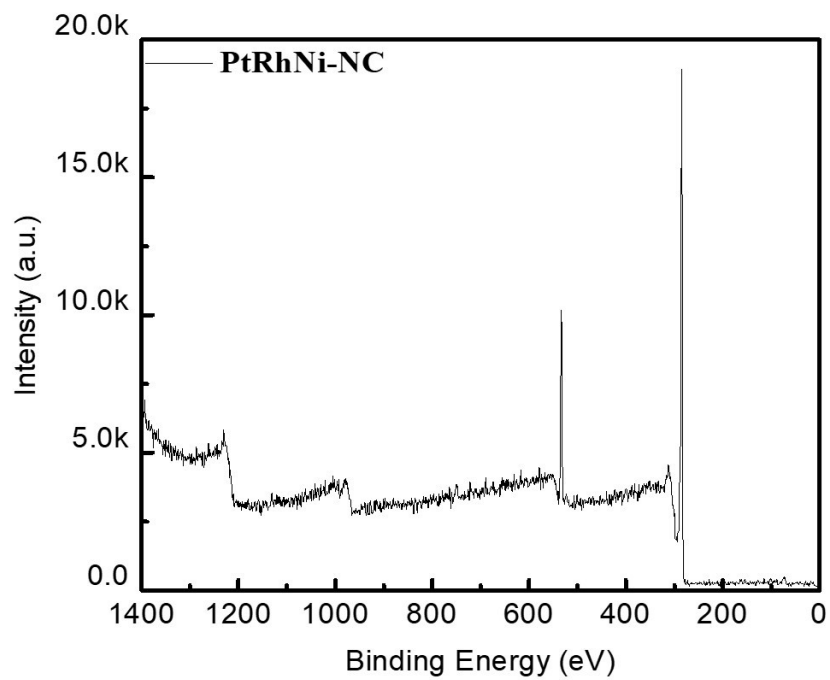


Figure S7. The Full XPS spectrum of PtRhNi NC.

11. The first two cycles of CO-stripping curves for Pt, Rh, PtRh and PtRhNi-NCs in 0.5 M H₂SO₄ electrolyte.

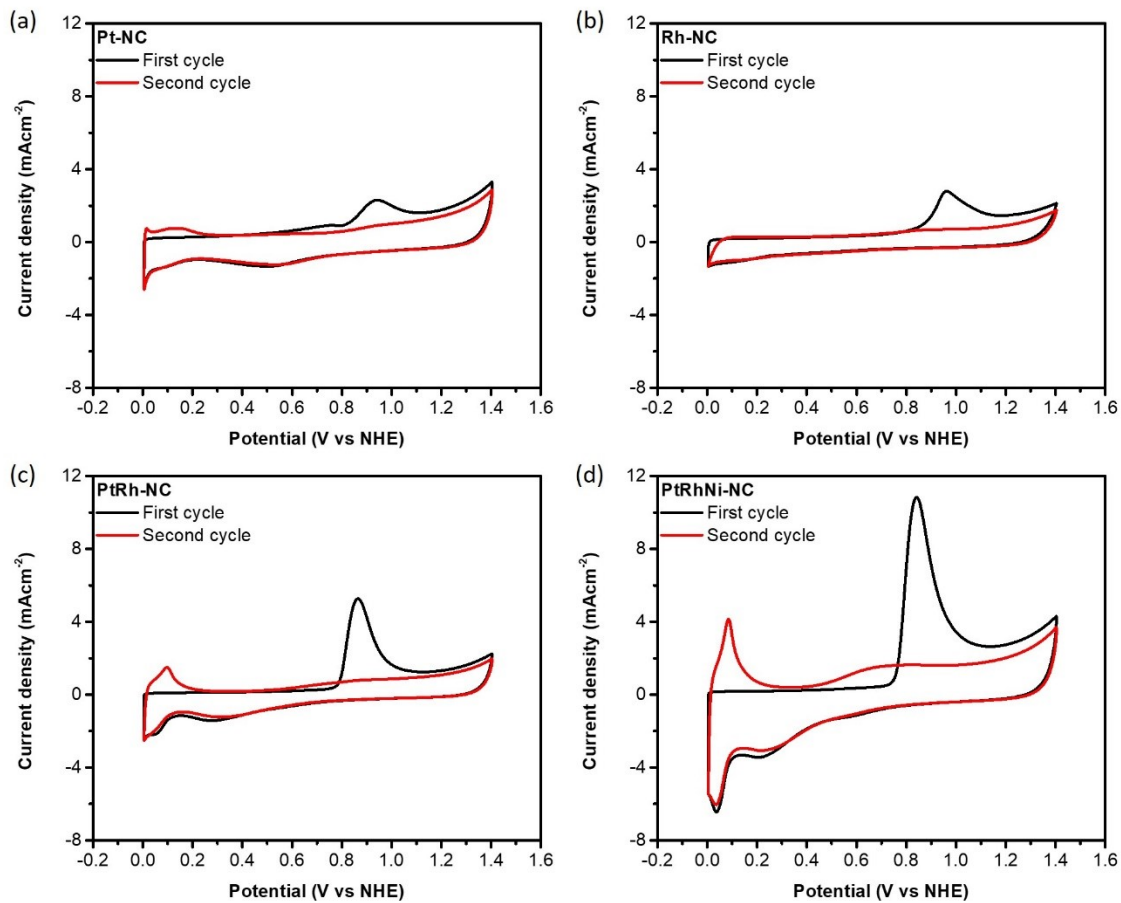


Figure S8. The CO-stripping curves of (a) Pt, (b) Rh, (c) PtRh and (d) PtRhNi NCs.

12. The mass activity of Pt, Rh, PtRh and PtRhNi-NCs in 0.5 M H₂SO₄ electrolyte.

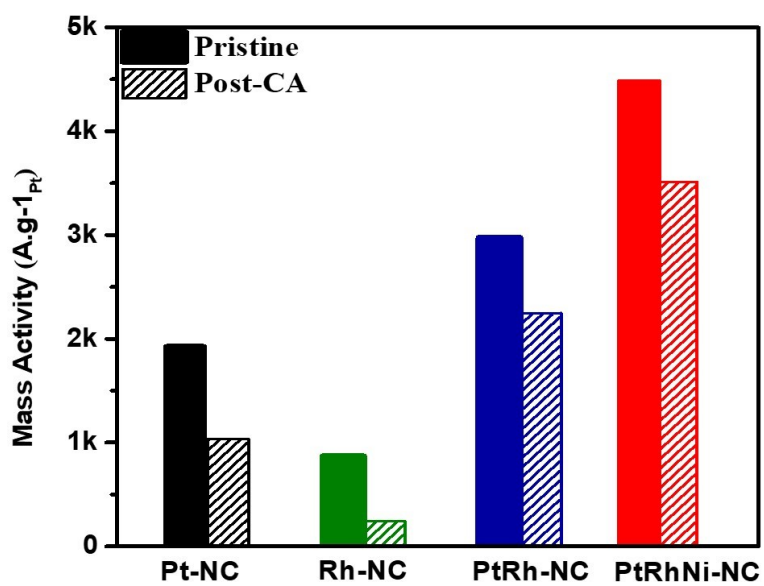


Figure S9. The mass activity of Pt, Rh, PtRh and PtRhNi-NCs in 0.5 M H₂SO₄ electrolyte.

13. The LSV curves of experimental NCs compared with commercial J.M.-Pt/C.

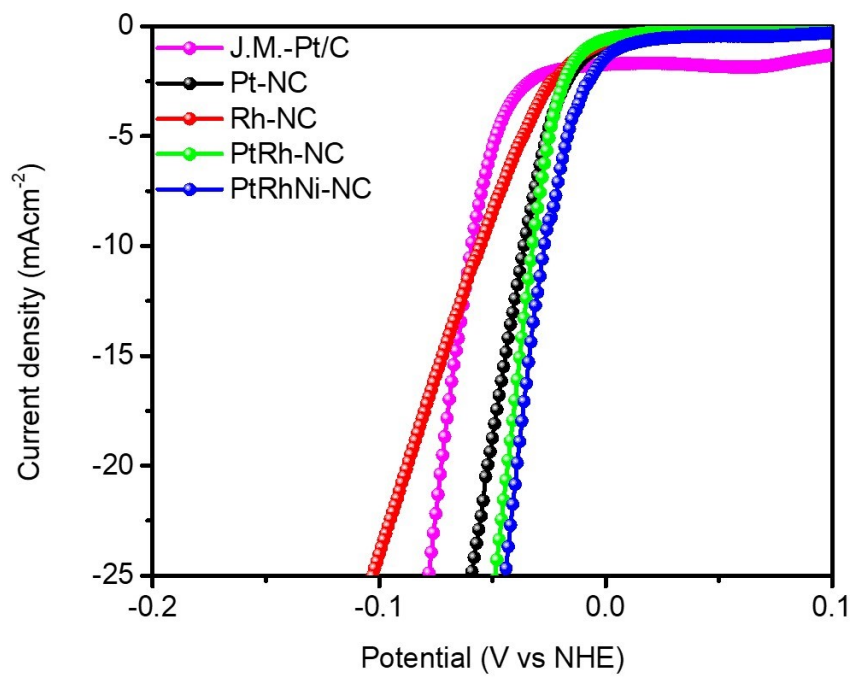


Figure S10. The LSV curves of experimental NCs compared with commercial J.M.-Pt/C.

14. CV curves of Pt, Rh, PtRh and PtRhNi NCs in 0.5 M H₂SO₄ electrolyte in pristine and post-CA conditions.

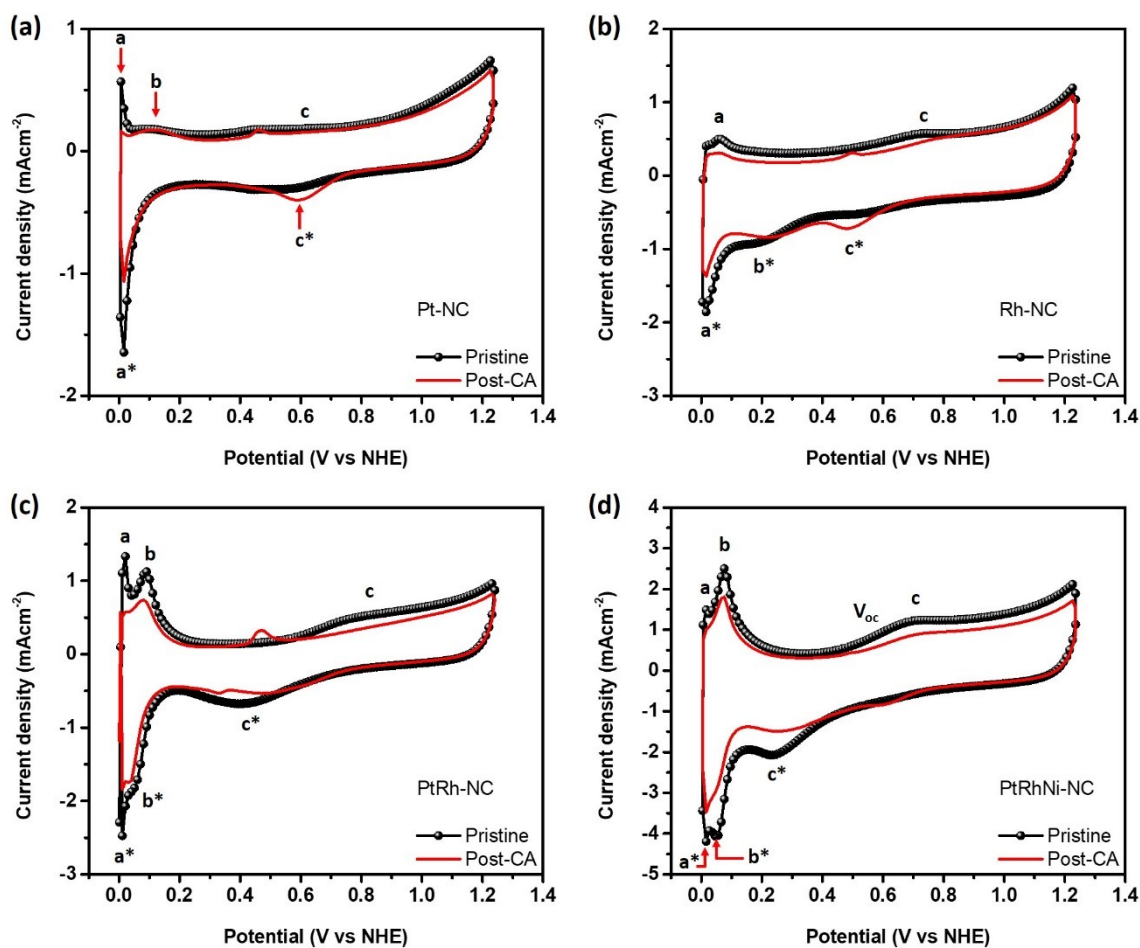
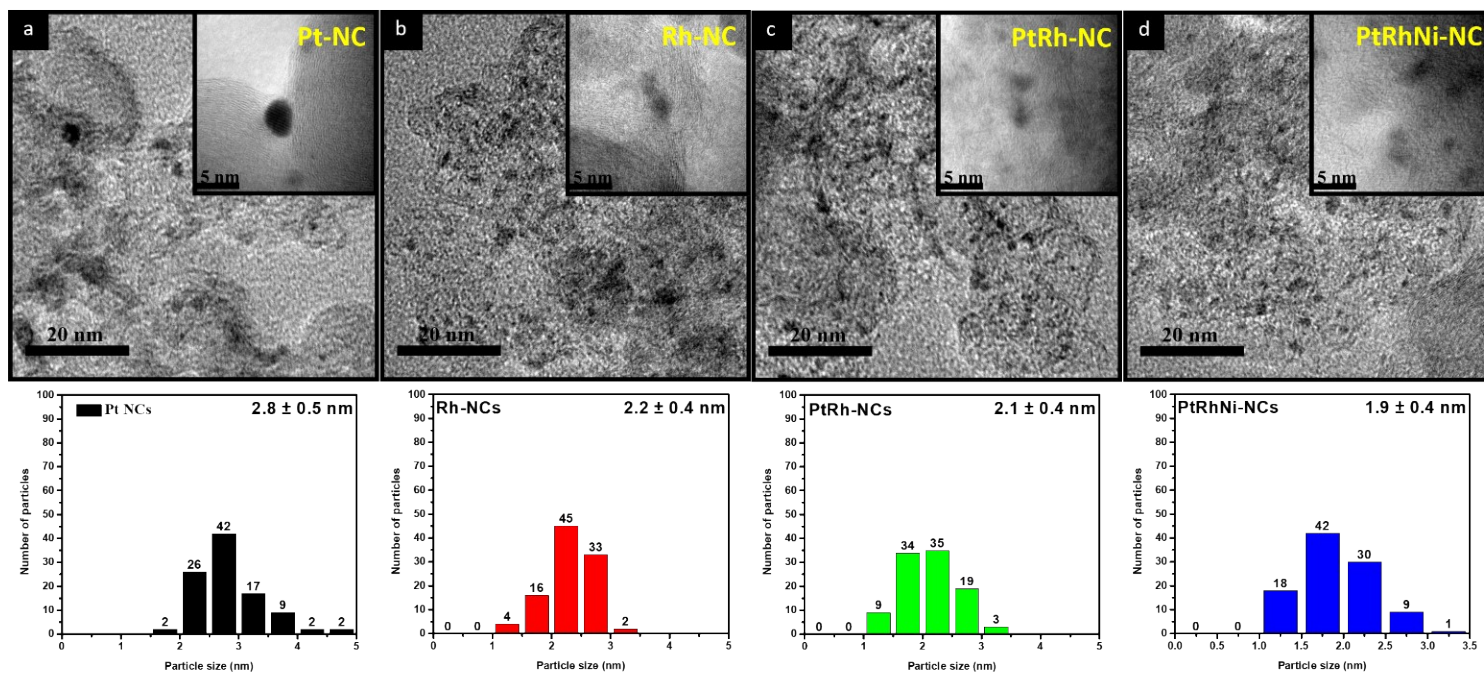


Figure S11. Pristine and post-CA CV curves of (a) Pt, (b) Rh, (c) PtRh and (d) PtRhNi NCs in 0.5 M H₂SO₄ electrolyte.

15. The HRTEM images of (a) Pt, (b) Rh, (c) PtRh and (d) PtRhNi NCs in 0.5 M H₂SO₄ electrolyte in



post-CA conditions.

Figure S12. The post-CA HRTEM images of (a) Pt, (b) Rh, (c) PtRh and (d) PtRhNi-NCs. Whereas, the corresponding low-resolution TEM images and particle size distribution histograms are shown in insets.

16. The mass activity of Pt, Rh, PtRh and PtRhNi-NCs in 0.5 M H₂SO₄ electrolyte.

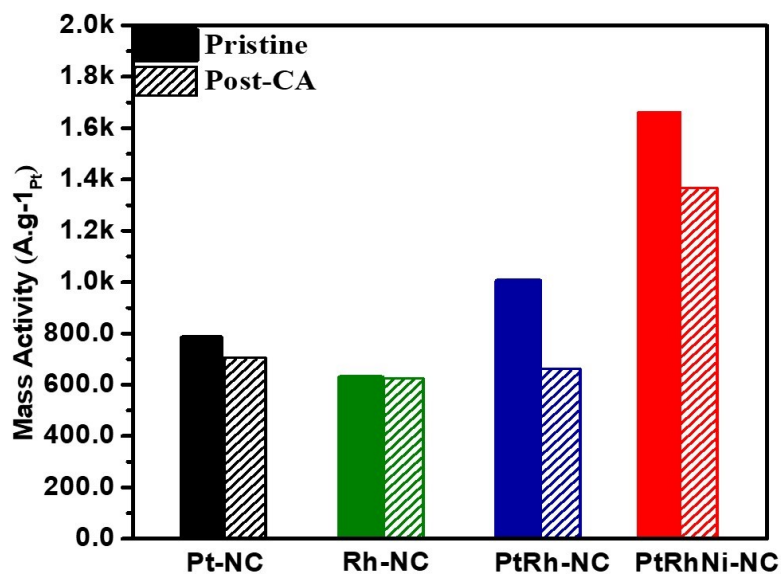


Figure S13. The mass activity of Pt, Rh, PtRh and PtRhNi-NCs in 0.5 M H₂SO₄ electrolyte.

17. CV curves of Pt, Rh, PtRh and PtRhNi-NCs in 1.0 M KOH electrolyte.

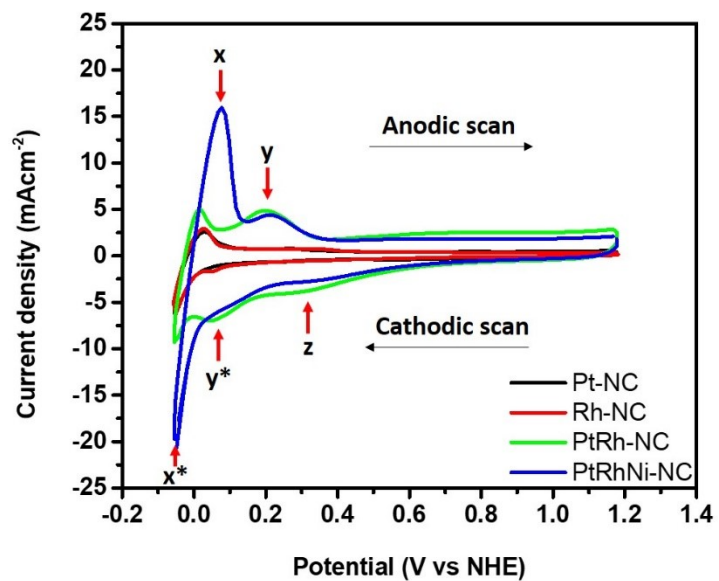


Figure S14. Superimposed CV curves of Pt, Rh, PtRh and PtRhNi-NCs in 1.0 M KOH electrolyte.

18. Pristine and post-CA CV curves of Pt, Rh, PtRh and PtRhNi NCs in 1.0 M KOH electrolyte.

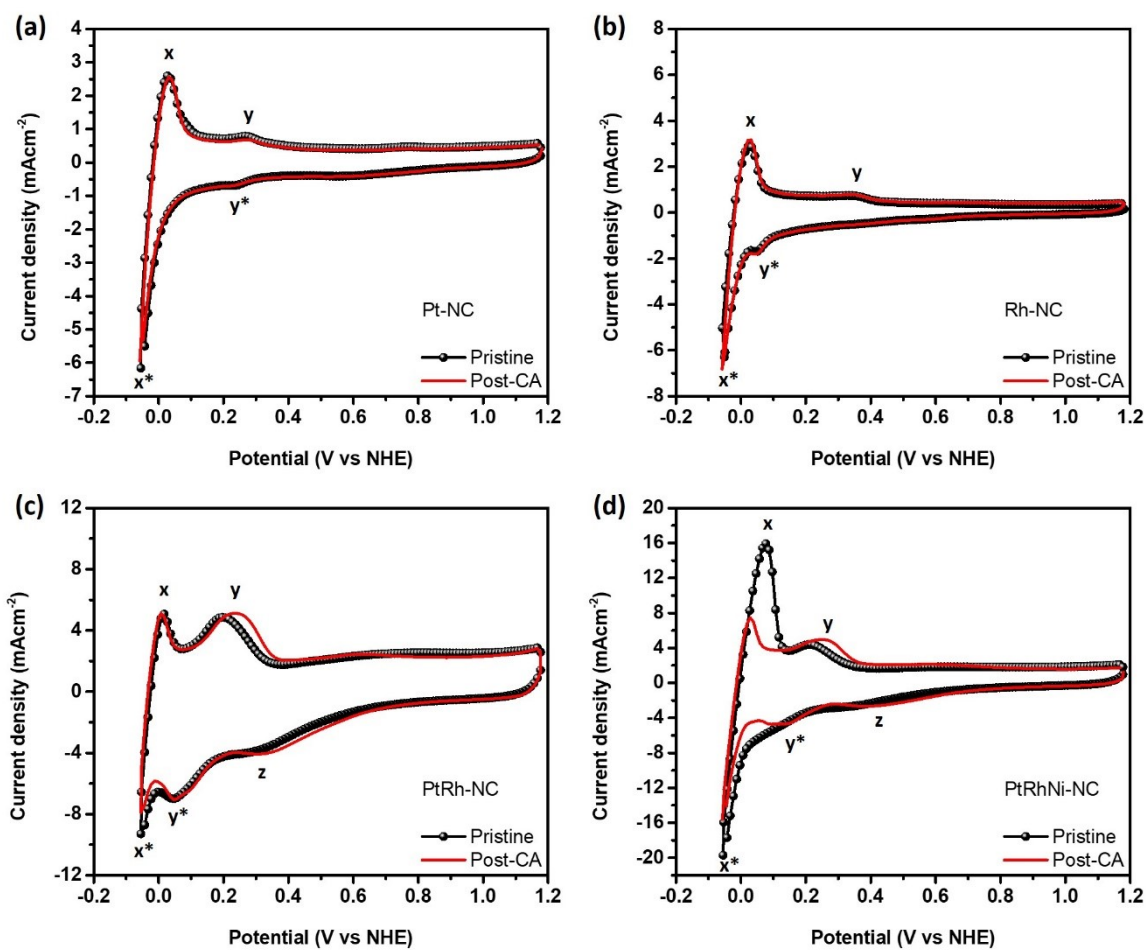


Figure S15. Pristine and post-CA CV curves of (a) Pt, (b) Rh, (c) PtRh and (d) PtRhNi NCs in 1.0 M KOH electrolyte.

19. HER performance of PtRhNi NC in a neutral medium.

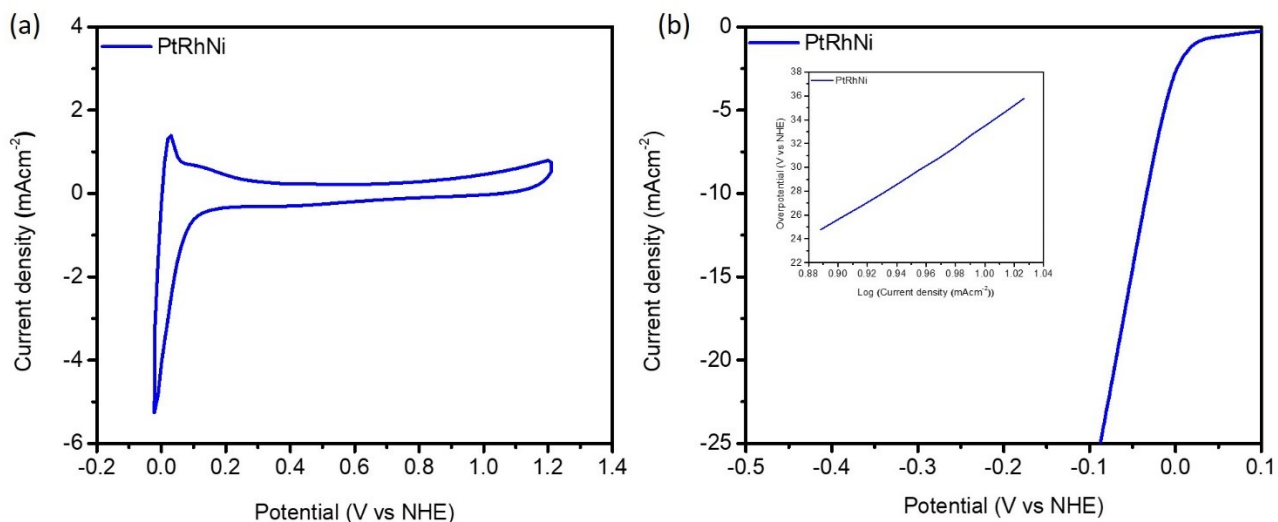


Figure S16. (a) The CV and (b) LSV curves of PtRhNi NC in a neutral environment (1.0 M PBS), whereas corresponding Tafel slope is depicted in the inset of Figure S16 b.

Table S2. The HER performance of PtRhNi NC in a neutral medium.

Sample	ECSA (m ² g ⁻¹)	η^* @ 10 mA cm ⁻² (mV)	Tafel slope (mV dec ⁻¹)	MA (A g _{Pt+Rh} ⁻¹)
PtRhNi	205	33	80	631

20. Benchmark of Pt-based catalysts in acidic HER.

Table S3. Benchmark of Pt-based catalysts in acidic HER.

Samples	Electrolyte, Scan rate	η_{10} (mV)	Tafel slope (mV/dec)	$MA_{0.05}$ (A/g _{Pt})	Reference
PtRhNi	0.5 M H ₂ SO ₄ ,	28	30	4489	This study.
PtRh	2 mVs ⁻¹	33	32	2972	
Pt/np-Co _{0.85} Se	0.5 M H ₂ SO ₄ , 50 mVs ⁻¹	58	26	1320 (at -100 mV)	1
Pd ₆₀ Pt ₄₀	0.5 M H ₂ SO ₄ , 5 mVs ⁻¹	130	N/A		2
Pt/NiS@Al ₂ O ₃	0.5 M H ₂ SO ₄ , 5 mVs ⁻¹	34	35		3
MO ₂ TiC ₂ T _x -Pt _{SA}	0.5 M H ₂ SO ₄ , 5 mVs ⁻¹	30	30		4
Pt-MoS ₂	0.1 M H ₂ SO ₄ , 0.2 2 mVs ⁻¹	150	96.0	N/A	5
Pt/MoS ₂ /CFs	0.5 M H ₂ SO ₄ , 5 mVs ⁻¹	80	53.6		6
Pt-SnOx NRs		48	33		7
Pt NRs		34	35		
5 ALD cycles Pt-WC	0.5 M H ₂ SO ₄ , 2 mVs ⁻¹	438	N/A		8
10 ALD cycles Pt-WC		408			
15 ALD cycles Pt-WC		306			
Pt ₁ /NPC	0.5 M H ₂ SO ₄ , 10 mVs ⁻¹	25	28	2860	9

* η_{10} refers to the overpotential at the cathodic current density of 10 mAcm⁻².

21. Benchmark of Pt-based catalysts in alkaline HER.

Table S4. Benchmark of Pt-based catalysts in alkaline HER.

Samples	Electrolyte	η_{10} (mV)	Tafel slope (mV/dec)	MA _{0.05} (A/g _{Pt})	Reference
PtRhNi	1.0 M KOH	28	73	1663	This study.
PtRh		57	76	1006	
Pt/np-Co _{0.85} Se		58	39	1280 (at -100 mV)	1
Pt/C		40	46	200 (at -100 mV)	1
PtSA-NT-NF		20	N/A	540 (at -100 mV)	10
er-WS2-Pt		48	65		11
Pt@PCM		139	73.6		12
PtSn ₄ single Crystal		37	39	N/A	13
Pt ₃ Ni frame/Ni(OH) ₂ /C		100	N/A		14

* η_{10} refers to the overpotential at the cathodic current density of 10 mAcm⁻².

22. Benchmark of Pt-based catalysts in neutral medium.

Table S5. Benchmark of Pt-based catalysts in neutral HER.

Catalysts	Electrolyte	η_{10} (mV)	Tafel slope (mV dec ⁻¹)	References
PtRhNi-NC	1.0 M PBS	33	80	This study
RhNiP MNs		44	88	15
RhCoB aerogel		113	149.1	16
RuP ₂ @NPC		57	87	17
Pt@NOMC-A		65	70	18
Rh ₅₀ Ru ₅₀ @UiO-66-NH ₂		111	93.4	19
OsP ₂ @NPC		54	82	20
PdP ₂ /CB		84.6	72.3	21
Ru-Co NPs@N-C		55	82	22

* η_{10} refers to the overpotential at the cathodic current density of 10 mAcm⁻².

References

1. K. Jiang, B. Liu, M. Luo, S. Ning, M. Peng, Y. Zhao, Y.-R. Lu, T.-S. Chan, F. M. F. de Groot and Y. Tan, *Nature Communications*, 2019, **10**, 1743.
2. R. Ojani, J. B. Raoof and E. Hasheminejad, *International Journal of Hydrogen Energy*, 2013, **38**, 92-99.
3. Y. Feng, Y. Guan, H. Zhang, Z. Huang, J. Li, Z. Jiang, X. Gu and Y. Wang, *Journal of Materials Chemistry A*, 2018, **6**, 11783-11789.
4. J. Zhang, Y. Zhao, X. Guo, C. Chen, C.-L. Dong, R.-S. Liu, C.-P. Han, Y. Li, Y. Gogotsi and G. Wang, *Nature Catalysis*, 2018, **1**, 985-992.
5. J. Deng, H. Li, J. Xiao, Y. Tu, D. Deng, H. Yang, H. Tian, J. Li, P. Ren and X. Bao, *Energy & Environmental Science*, 2015, **8**, 1594-1601.
6. D. Hou, W. Zhou, X. Liu, K. Zhou, J. Xie, G. Li and S. Chen, *Electrochimica Acta*, 2015, **166**, 26-31.
7. T.-H. Huang, D. Bhalothia, S. Dai, C. Yan, K.-W. Wang and T.-Y. Chen, *Sustainable Energy & Fuels*, 2021, **5**, 2960-2971.
8. I. J. Hsu, Y. C. Kimmel, X. Jiang, B. G. Willis and J. G. Chen, *Chemical Communications*, 2012, **48**, 1063-1065.
9. T. Li, J. Liu, Y. Song and F. Wang, *ACS Catalysis*, 2018, **8**, 8450-8458.
10. L. Zhang, L. Han, H. Liu, X. Liu and J. Luo, *Angewandte Chemie International Edition*, 2017, **56**, 13694-13698.
11. K. Tang, X. Wang, Q. Li and C. Yan, *Advanced Materials*, 2018, **30**, 1704779.
12. H. Zhang, P. An, W. Zhou, B. Y. Guan, P. Zhang, J. Dong and X. W. Lou, *Science Advances*, 2018, **4**, eaao6657.
13. G. Li, C. Fu, W. Shi, L. Jiao, J. Wu, Q. Yang, R. Saha, M. E. Kamminga, A. K. Srivastava, E. Liu, A. N. Yazdani, N. Kumar, J. Zhang, G. R. Blake, X. Liu, M. Fahlman, S. Wirth, G. Auffermann, J. Gooth, S. Parkin, V. Madhavan, X. Feng, Y. Sun and C. Felser, *Angewandte Chemie International Edition*, 2019,

58, 13107-13112.

14. C. Chen, Y. Kang, Z. Huo, Z. Zhu, W. Huang, H. L. Xin, J. D. Snyder, D. Li, J. A. Herron, M. Mavrikakis, M. Chi, K. L. More, Y. Li, N. M. Markovic, G. A. Somorjai, P. Yang and V. R. Stamenkovic, *Science*, 2014, **343**, 1339.
15. Q. Mao, S. Jiao, K. Ren, S. Wang, Y. Xu, Z. Wang, X. Li, L. Wang and H. Wang, *Chemical Engineering Journal*, 2021, **426**, 131227.
16. K. Deng, T. Ren, Y. Xu, S. Liu, Z. Dai, Z. Wang, X. Li, L. Wang and H. Wang, *Journal of Materials Chemistry A*, 2020, **8**, 5595-5600.
17. Z. Pu, I. S. Amiin, Z. Kou, W. Li and S. Mu, *Angewandte Chemie International Edition*, 2017, **56**, 11559-11564.
18. Y. Yin, T. Liu, D. Liu, Z. Wang, Q. Deng, D. Qu, Z. Xie, H. Tang and J. Li, *Journal of Colloid and Interface Science*, 2018, **530**, 595-602.
19. Z. Ding, K. Wang, Z. Mai, G. He, Z. Liu and Z. Tang, *International Journal of Hydrogen Energy*, 2019, **44**, 24680-24689.
20. S. Chakrabarty, B. K. Barman and C. Retna Raj, *Chemical Communications*, 2019, **55**, 4399-4402.
21. F. Luo, Q. Zhang, X. Yu, S. Xiao, Y. Ling, H. Hu, L. Guo, Z. Yang, L. Huang, W. Cai and H. Cheng, *Angewandte Chemie International Edition*, 2018, **57**, 14862-14867.
22. S. Yuan, Z. Pu, H. Zhou, J. Yu, I. S. Amiin, J. Zhu, Q. Liang, J. Yang, D. He, Z. Hu, G. Van Tendeloo and S. Mu, *Nano Energy*, 2019, **59**, 472-480.